

Two-point observations of low-frequency waves at 67P/Churyumov-Gerasimenko during descent of PHILAE: Comparison of RPCMAG and ROMAP

I. Richter¹, H.-U. Auster¹, G. Berghofer², C. Carr³, E. Cupido³, K.-H. Fornacon¹, C. Goetz¹, P. Heinisch¹, C. Koenders¹, B. Stoll¹, B.T. Tsurutani⁴, C. Vallat⁵, M. Volwerk², and K.-H. Glassmeier¹

¹Institut für Geophysik und extraterrestrische Physik, TU Braunschweig, Mendelssohnstr. 3, 38106 Braunschweig, Germany.

²Institut für Weltraumforschung, Schmiedlstraße 6, 8042 Graz, Austria

³Imperial College London, Exhibition Road, London SW7 2AZ, UK.

⁴Jet Propulsion Laboratory, California Institute of Technology, 4800 Oak Grove Drive Pasadena, CA 91109, USA.

⁵Rosetta Science Ground Segment, European Space Astronomy Centre, 28691 Villanueva de la Cañada, Madrid, Spain.

Correspondence to: Ingo Richter (i.richter@tu-braunschweig.de)

Abstract. The European Space Agency’s spacecraft ROSETTA has reached its final destination, comet 67P/Churyumov-Gerasimenko. Whilst orbiting in the close vicinity of the nucleus the ROSETTA magnetometers detected a new type of low-frequency waves possibly generated by a cross-field current instability due to freshly ionized cometary water group particles. During separation, descent and landing of the lander PHILAE on comet 67P/Churyumov-Gerasimenko, we used the unique opportunity to perform combined measurements with the magnetometers onboard ROSETTA (RPCMAG) and its lander PHILAE (ROMAP). New details about the spatial distribution of wave properties along the connection line of the ROSETTA orbiter and the lander PHILAE are revealed. An estimation of the observed amplitude, phase and wavelength distribution will be presented as well as the measured dispersion relation, characterizing the new type of low-frequency waves. The propagation direction and polarization features will be discussed using the results of a minimum variance analysis. Thoughts about the size of the wave source will complete our study.

1 Introduction

After a 10 year flight the ROSETTA spacecraft (Glassmeier *et al.*, 2007a) arrived at its final target comet 67P/Churyumov-Gerasimenko (67P/C-G) in August 2014. At that time 67P/C-G was at a heliocentric distance of about 3.6 AU and its gas production rate was about $2 \cdot 10^{25} \text{ s}^{-1}$ as reported by Gulkis *et al.* (2015). Neither any major plasma regions/boundaries were developed, nor a bowshock or a magnetic cavity formed at that time. Therefore, only plasma interactions of a weak comet as

described by e.g. *Rubin et al.* (2014) were expected in sharp contrast to the flybys at the more active
20 comets 1P/Halley (*Neubauer et al.*, 1986), 26P/Grigg-Skjellerup (*Neubauer et al.*, 1993; *Glassmeier
and Neubauer*, 1993), 21P/Giacobini-Zinner (*Smith et al.*, 1986), and 19P/Borrelly (*Richter et al.*,
2011).

Nevertheless the orbiter magnetometer RPCMAG observed magnetic, low-frequency waves with
frequencies around 30 – 50 mHz and relative amplitudes up to about $\delta B/B \sim 1 - 2$
25 (*Richter et al.*, 2015) almost continuously since ROSETTA had reached a distance of about 100
km to 67P/C-G in August 2014. These waves and their generation mechanism are clearly distinct
from waves observed at other comets (e.g. *Volwerk et al.*, 2014; *Glassmeier et al.*, 1989).

In the months after arrival at 67P/C-G, ROSETTA operated under different conditions and at
various distances to the comet. Thus, a comprehensive insight into the frequency and amplitude
30 characteristics of these waves may be gained. No information, however, could be retrieved on the
wavelengths, velocities and the dispersion relation as only single-point observations were available.
This situation changed during separation, descent (and rebound) and landing (SDL) of the ROSETTA
lander PHILAE on November 12, 2014. During the 1.5 days of joint operations of the orbiter mag-
netometer RPCMAG (*Glassmeier et al.*, 2007b) and the lander magnetometer ROMAP (*Auster et*
35 *al.*, 2007), wave observations at two different, spatially changing locations, were made which allow
to deduce wavelength, velocity and propagation information as well.

In this paper we will give a short overview of the ROSETTA mission and the plasma instrumen-
tation in section 2. Section 3 includes the temporal and spatial evolution of wave properties and thus
extends the findings presented in *Richter et al.* (2015) using also later observations. Particularly the
40 energy density in a certain frequency band is a well-proven means to characterize waves properties
and to compare wave observations made by different instruments at different locations. A detailed
description of the SDL phase with its changing s/c separation distance and combined orbiter-lander
observations, concentrating on the time interval between separation and landing of PHILAE, is pre-
sented in section 4. Section 5 contains a example of a joint RPCMAG / ROMAP wave observation
45 and an illustration of the high correlation of the detected waves. The frequency distribution of the
waves will be analyzed as well as the spatial separation dependence of the measured wave ampli-
tudes. The extended treatment of our measurements including correlation techniques will lead us to
the determination of the two point wave phase relations and the estimation of wavelengths. With
knowledge of these parameters a dispersion relation of the observed waves can be determined. A
50 minimum/maximum-variance analysis reveals propagation properties.

As all measurements and analysis techniques are affected by certain errors a systematic error
estimation is given in section 6 in order to be able to draw the right conclusions in section 7.

2 Mission overview and instrumentation

ESA's comet chaser mission ROSETTA (*Glassmeier et al., 2007a*) - launched in March 2004 - is
55 designed for long-term cometary science studies in various scientific disciplines. After four plan-
etary swingbys, two asteroid flybys, and a two and a half year hibernation period, ROSETTA was
successfully turned on again in January 2014. After several innovative orbital manoeuvres it reached
its target comet 67P/C-G on August 6, 2014 at a heliocentric distance of 3.6 AU. Unlike former
cometary missions such as GIOTTO to comet 1P/Halley (*Neubauer et al., 1986*) and 26P/Grigg-
60 Skjellerup (*Neubauer et al., 1993; Glassmeier and Neubauer, 1993*), ICE to 21P/Giacobini-Zinner
(*Smith et al., 1986*) and DS1 to comet 19P/Borrelly (*Richter et al., 2011*) the Rosetta mission re-
mained close to the comet nucleus ($\sim 10 - 250$ km) for several months with relative velocities less
than 1 m/s.

As not only observations in close vicinity of the target body but also measurements on the surface
65 of 67P/C-G were intended to be conducted, the ROSETTA mission was designed to comprise two
spacecrafts: an orbiter observing the comet in varying distances between a few kilometers up to a few
hundred kilometers, and the Lander PHILAE, performing measurements on the surface of 67P/C-
G. PHILAE was successfully separated from the orbiter on November 12, 2014 at 08:35 UTC and
performed its final landing at 17:31 UTC (*Heinisch et al., 2015*) after nine hours of descent. At the
70 time of the landing 67P/C-G was at a heliocentric distance of 2.99 AU (*Biele et al., 2015*). **The
cometary activity over the August to November 2014 time period remained nearly constant, with a
gas production rate of $\sim 1 \cdot 10^{26} \text{s}^{-1}$ (*Bieler et al., 2015*).**

As ROSETTA is supposed to investigate plasma-physical properties in the surroundings and on
the surface of 67P/C-G, it is equipped with two plasma packages, each of which containing a magne-
75 tometer experiment. The ROSETTA Plasma Consortium (RPC) (*Carr et al., 2007*) is a suite of five
plasma sensors onboard the orbiter, and the ROMAP instrument (*Auster et al., 2007*) is a double-
featured sensor comprising of a magnetometer and a plasma-monitor located on PHILAE.

The RPCMAG instrument, as part of RPC, comprises of two triaxial fluxgate **magnetometer** sen-
sors (FGM) (*Glassmeier et al., 2007b*) which are mounted on a 1.5 m long boom outside the or-
80 biter, separated from each other by 15 cm. Due to this short boom, the small separation distance
and a magnetically heavily polluted spacecraft, the magnetic field data were strongly disturbed by
thrusters, transient currents, reaction wheel movements and heater currents. Therefore, removal of
the time varying magnetic disturbance fields was a difficult task and data interpretation has to be
conducted very carefully. RPCMAG can measure fields up to ± 16000 nT with a resolution of 31 pT
85 and a maximum sampling rate of 20 magnetic field vectors per second (burst mode).

The low-frequency waves, being the object of this study, occur in a frequency range ($\sim 20 -$
50 mHz) where the contamination with spacecraft bias fields plays an insignificant role. We use
RPCMAG data of the highest available calibration and cleaning level for our analyses: ground cali-
bration results have been applied and furthermore the frequency dependent influence of ROSETTA's

90 four rotating reaction wheels has been eliminated successfully. This was possible by knowledge of
the wheel rotation frequencies which are provided as spacecraft-housekeeping parameters every 32 s.
In the magnetic field raw data the wheel disturbance of ~ 2 nT peak-to-peak amplitude occurred in
the measurement baseband (0-10 Hz, mainly in the band above 1 Hz) as image frequencies of the
original rotation frequencies (up to 1500 rpm) by multiple mirroring at the Nyquist frequency. The
95 elimination was performed in the frequency domain by reducing the amplitude at the expected dis-
turbance frequency down to the level of the surrounding spectral neighborhood of the regarded data
point. Calibration of the data and cleaning algorithms were employed to ensure that our analysis
reveals real plasma effects and does not deal with spacecraft generated signatures.

The ROMAP magnetometer (*Auster et al.*, 2007) onboard PHILAE is a single triaxial FGM sensor
100 located on a 60 cm boom which was deployed roughly an hour after PHILAE was separated from
the orbiter. ROMAP can measure fields up to ± 2000 nT with a resolution of 10 pT and a maximum
sampling rate of 64 vectors per second. Due to operational constraints ROMAP had to be operated
with the low vector rate of 1 Hz during SDL.

3 Evolution of wave activity deduced from long-term RPCMAG observations

105 The magnetometer is designed to be a low power consuming instrument which also generates only
a small amount of telemetry packages. Therefore, RPCMAG has been allowed to operate almost
continuously since spring 2014 while ROSETTA was still at about one million km away from the
target comet. Thus, measurements spanning one year are available in order to study the new wave
phenomena. All magnetic field observations described in this work are presented in the Cometary-
centered Solar Equatorial-coordinate system (CSEQ). Here the $+x$ -axis points from the comet to the
110 Sun, the $+z$ -axis is the component of the Sun's north pole of date orthogonal to the $+x$ -axis, and
the $+y$ -axis completes the right-handed reference frame. The origin of the coordinate system is the
comet's center of mass. All celestial-geometrical calculations were performed using the versatile
SPICE system (*Acton*, 1996). All errors given in this work are stated as error of the mean value, i.e.,
115 standard deviation divided by the square root of the number of datapoints.

Using the RPCMAG instrument we started to detect low-frequency waves at the beginning of Au-
gust 2014 at a distance of ~ 100 km to 67P/C-G (*Richter et al.*, 2015). In the meantime several months
of successful operations were conducted allowing for a more detailed statistical analysis. Fig. 1 il-
lustrates an example of well developed magnetic field waves observed by RPCMAG on January 8,
120 2015 between 22:00 and 22:15 UTC. The spacecraft was operating at a distance of ~ 27.5 km from
the nucleus at that time. The shown waves are characterized by amplitudes of ~ 6 nT, a $\delta B/B \sim 1$
, and frequencies of ~ 28 mHz. These amplitude and frequency values are typical for the newly
detected low-frequency waves at 67P/C-G and first described by (*Richter et al.*, 2015).

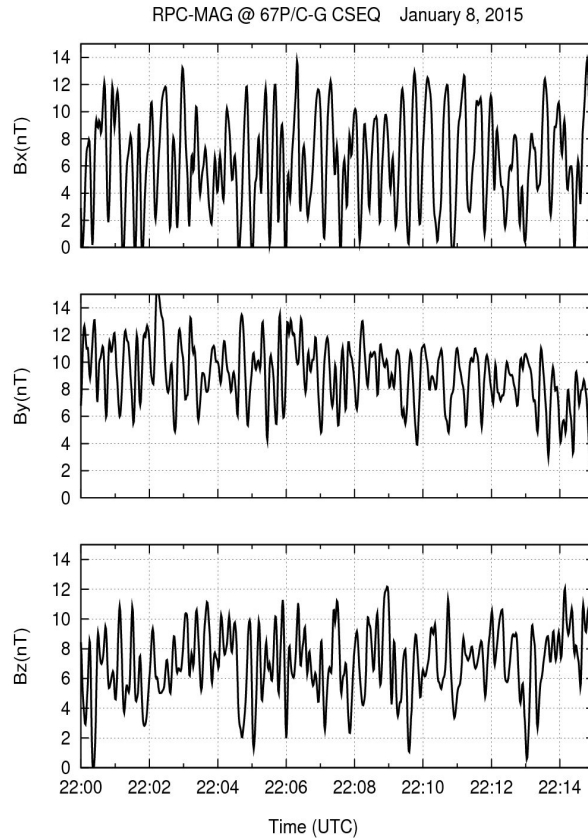


Figure 1. Magnetic field measurements made by RPCMAG on January 8, 2015, 22:00 - 22:15 UTC, as an example for the detection of low-frequency waves. **Large-amplitude waves with a frequency of 28 mHz are clearly visible.** The spacecraft position at that time was (0.2, -27, 5) km in the CSEQ-coordinate system.

In order to systematically investigate the temporal and spatial evolution of the wave activity, the energy density in the 10 - 100 mHz band has been calculated **by integrating the** power spectral density for almost 9000 hourly intervals. **As result** Fig. 2 shows the radial dependence of the wave activity represented as the logarithm of the wave energy density as a function of spacecraft comet distance. **The plot covers the first part of the ROSETTA's comet phase between May 2014 and April 2015 continuously.**

As expected, measurements sampled from the solar wind over the time period of May-Aug 2014 (violet part) revealed very low and featureless energy density levels. However, the onset of wave activity at ~ 100 km altitude from the Comet's surface is associated with an abrupt increase of the energy density that persists up to the point that ROSETTA reached at a distance of 10 km in October 2014 (blue part).

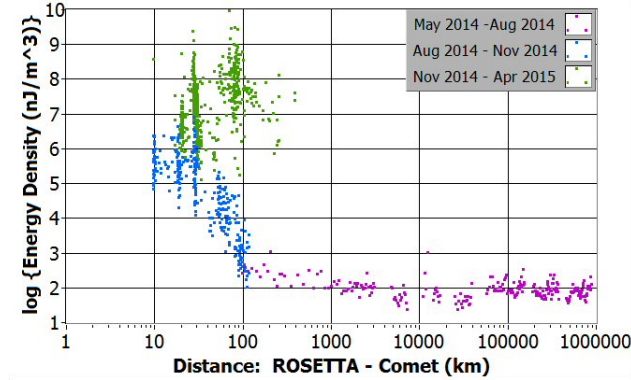


Figure 2. The energy density of the observed waves in dependence of the radial distance between ROSETTA and 67P/C-G for one year of observations. Time segments are color-coded.

135 **Over the following months, between November 2014 and April 2015**, ROSETTA moved again to larger distances (green part). However, as seen in Fig. 2, the energy density does not decrease again. This clearly indicates that wave activity strongly depends not only on radial distance to the nucleus but also on cometary activity which increased in the following months due to a decreasing comet-sun distance. A measure for the cometary activity is the gas production rate which increased
 140 by a factor of 3 from $1.5 \cdot 10^{26} \text{ s}^{-1}$ in November 2014 to $4.5 \cdot 10^{26} \text{ s}^{-1}$ in March 2015 according to K.C. Hansen (personal communication).

4 Joint RPCMAG-ROMAP observations

At November 12, 2014 - the day of landing - we had the unique opportunity of operating the two ROSETTA magnetometers in parallel at different locations. Thus, we use the descent phase of PHILAE to collect magnetic field data with both instruments, compare the waves detected with both
 145 sensors and analyze the relative wave phase shifts in order to estimate wavelength and wave velocity.

On November 12, 2014 at 08:35 UTC PHILAE separated from ROSETTA. This occurred at a distance of ~ 22.38 km from the comet (*Biele et al.*, 2015). PHILAE veered away from the orbiter with
 150 a relative velocity of ~ 0.7 m/s. The temporal evolution of the radial distance between both spacecraft is shown in Fig. 3. **The descent of PHILAE lasted for ~ 7 hours, while its first touchdown occurred at 15:34 UTC at a distance of ~ 15 km from ROSETTA. PHILAE experienced two more ground contacts at 16:20 UTC and 17:25 UTC before it settled in a fixed location on the comet's surface at 17:31 UTC (*Auster et al.*, 2015). During PHILAE's journey, ROSETTA was slowly moving away
 155 from the comet.**

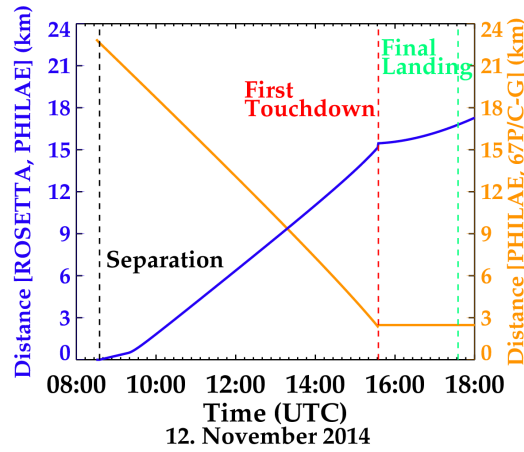


Figure 3. Temporal evolution of the distance between ROSETTA and PHILAE and also between PHILAE and 67P/C-G (center) during the descent to 67P/C-G on November 12, 2014. The shown trajectories have been generated using nominal kernels as the reconstructed SPICE kernels are not available yet.

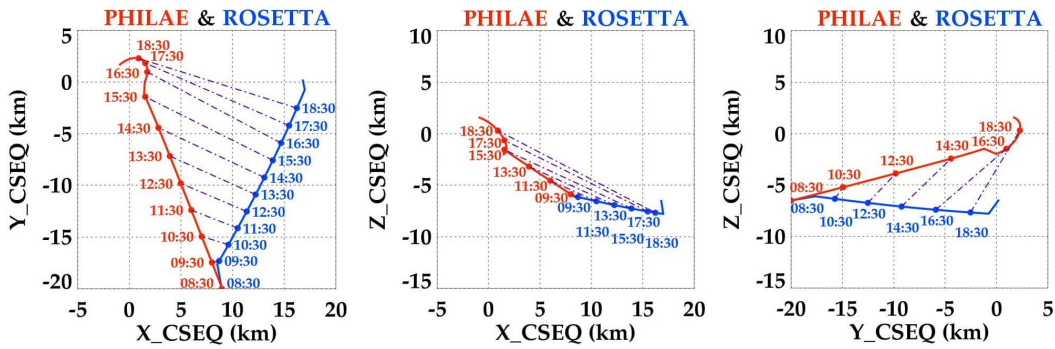


Figure 4. Projection of the two spacecraft trajectories in the xy -, xz -, and yz -planes of the CSEQ-system during the SDL phase. PHILAE's trajectory (red) and ROSETTA'S trajectory (blue) are shown including time-tags. The violet dash-dotted lines illustrate the orbiter-lander connecting lines at selected times. The data were derived from nominal SPICE kernels.

Fig. 4 exhibits the separation and descent scenario in more detail. The projected trajectories of both spacecraft including time-tags and the connecting lines between ROSETTA and PHILAE illustrate the spatio-temporal development of the spacecraft movements. During PHILAE's descent to 67P/C-G the distance between the vehicles increased continuously. The arc-like motion of PHILAE after 17:31 UTC is due to the common rotation with the comet.

A closer look at the direction of the shown **imaginary lines connecting the two spacecraft** reveals that **these lines are constantly parallel over** the time of descent. This important geometrical feature will be **considered later during the estimation of the projected wavelength and the determination of the wave direction**. In this context also the mean background field measured by RPCMAG shall be
165 taken into account. **It can be calculated by averaging the measured field over certain time intervals**. From the background field point of view the descent phase can be split into three major time intervals showing three different field configurations:

$\langle \mathbf{B}_0 \rangle = (-5.5, -0.1, 4.6) \pm (0.02, 0.02, 0.02)$ nT from 10:20 - 12:40 UTC,

$\langle \mathbf{B}_0 \rangle = (-3.6, -5.3, 7.9) \pm (0.02, 0.03, 0.02)$ nT from 12:50 - 16:00 UTC and finally

170 $\langle \mathbf{B}_0 \rangle = (-0.3, -0.8, 0.4) \pm (0.03, 0.03, 0.03)$ nT from 16:00 - 18:00 UTC. These values imply that the average angles between background field and the orbiter-lander connecting line changed as well and are given by $(154.5^\circ \pm 0.3^\circ)$, $(112.3^\circ \pm 0.14^\circ)$, $(98.0^\circ \pm 1.85^\circ)$ for the three time intervals. One can see that this angle follows a decreasing trend, meaning that the background field rotates against a direction perpendicular to the orbiter-lander connecting line. The average angle is roughly
175 about 121° .

During SDL the orbiter magnetometer RPCMAG was permanently operating at 20 Hz sampling rate whereas the lander magnetometer ROMAP was operated at 1 Hz sampling rate. Due to this operational constraint the RPCMAG data had to be undersampled to an effective sample rate of 1 Hz in order to be directly comparable with ROMAP data. This reduction is done by just picking out
180 every 20th raw vector and resampling the data in order to be aligned to the ROMAP time tags.

To eliminate the effects imposed by internal s/c disturbance sources to the magnetic field data, a 1st order Butterworth-bandpass filter *Butterworth (1930)* was applied in the 10-100 mHz range. This technique allows us to concentrate in the frequency range of 20-50 mHz that is the main interest of our analysis.

185 **It should be noted that the lander attitude, i.e. the orientation of the Lander frame, in which the ROMAP data were measured, was primarily unknown during descent and landing as it could not be linked to any celestial coordinate system of reference.** However, correlating RPCMAG and ROMAP data and rotating the ROMAP data to the RPCMAG system using a fit algorithm for minimizing the deviation of both datasets as described by *Heinisch et al. (2015)*, **allows the determination of the**
190 **lander attitude and the transformation of the ROMAP data to the CSEQ system as well.** However, the attitude can not be calculated for all times during SDL, as on the one hand the correlation between RPCMAG and ROMAP is not high enough for certain intervals and on the other hand the complex rotation/nutation/precession of PHILAE **precludes** a proper derivation of geometrical parameters. Therefore, ROMAP data **are** available in a celestial linked coordinate system for selected intervals
195 only. An impression of the manifold movement during descent can be received from the video sequence of the reconstructed flight (*Heinisch and Finke, 2015*). The available attitudes during descent

and landing are in excellent agreement to OSIRIS¹ and CONSERT² observations (*Sierks et al.*, 2015) as well as to the SONC³ calculations (*Jurado et al.*, 2016), giving us additional confidence that we have the correct orientations.

200 5 Observational results

An example of joint magnetic field registration

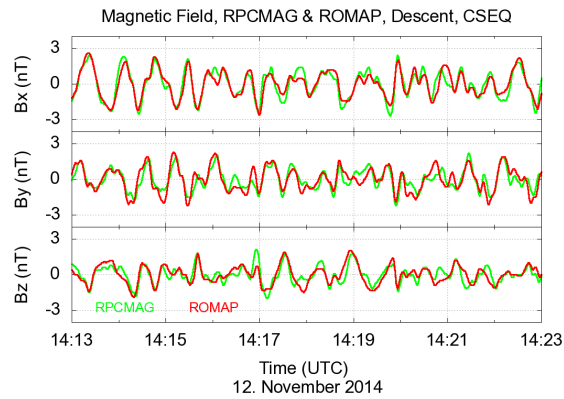


Figure 5. An example of 10 minutes parallel measurements of RPCMAG & ROMAP data during the PHILAE descent. Waves with frequencies of ~ 30 mHz can clearly be seen in both time series.

¹Camera experiment onboard ROSETTA

²Comet Nucleus Sounding Experiment onboard ROSETTA & PHILAE

³Science and Operation Navigation Center, Toulouse, France

Fig. 5 shows a typical example of a processed magnetic field time series. Here all three magnetic field components measured by RPCMAG (green) and ROMAP (red) are displayed together within a 10 minute interval on November, 12 at 14:13 – 14:23 UTC. This interval illustrates the typical behavior of the magnetic field during SDL. At this time the distance between PHILAE and ROSETTA was ~ 11.5 km, and PHILAE was still ~ 6.5 km away from the center of 67P/C-G.

Waves with frequencies of ~ 30 mHz can clearly be seen in both time series. The amplitudes of the waves at this time are roughly the same and the waves seen here are well-correlated, which means that the instruments are operating in the same plasma environment and scanning the same wave field.

210 Correlation of the observed waves

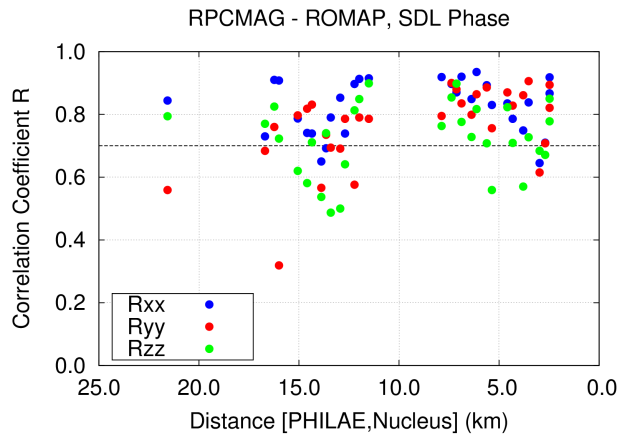


Figure 6. Correlation coefficients R_{xx} (blue), R_{yy} (red) and R_{zz} (green) of the six magnetic field components measured by RPCMAG and ROMAP. Correlation has been calculated using moving 300 s intervals and plotted versus the lander-comet distance. The horizontal line at $R=0.7$ designates the usual lower confidence level.

The magnetic field data of the 10 min time interval presented in Fig.5 already indicates that magnetic measurements of both instruments are highly correlated during the SDL phase. A detailed correlation survey of pairwise analyzed components from both instruments ($B_x^{\text{ROMAP}}, B_x^{\text{RPCMAG}}$), ($B_y^{\text{ROMAP}}, B_y^{\text{RPCMAG}}$), ($B_z^{\text{ROMAP}}, B_z^{\text{RPCMAG}}$) confirms their high degree of correlation (Fig.6). The Pearson correlation coefficients R_{xx} (blue), R_{yy} (red) and R_{zz} (green) of the six magnetic field components are plotted versus the lander-comet distance, for all times, where data of both instruments are available. This analysis has been performed on moving, not overlapping 300 s intervals in order to investigate the datasets with a suitably granularity of time. Furthermore the data have been shifted against each other in order to find the maximum correlation. The required shift of the individual intervals is in the order -2 s – $+0.5$ s without evidence of a unique pattern. The obtained results show that for 67 analyzed intervals the correlation coefficients are above 0.7, while only 21 exhibit correlations

below 0.7. This indicates that in 76 % of all cases where data are available, our separated instruments detected collective plasma structures and waves.

225 A rough estimate of the correlation length $l_c = \tau_c v$ can be calculated with knowledge of the coherence time τ_c and a typical propagation velocity v . The coherence time τ_c is the time lag for which the modulus of the normalized cross correlation function is decayed to $1/e$. From the analysis we obtain maximum coherence times of $\tau = 8$ s. A typical wave propagation velocity is the phase velocity v_p . As shown further down this is about (6.1 ± 0.8) km/s in the present regime. Thus, the coherence length becomes roughly 48 km which is above the maximum orbiter/lander separation distance.

230 **Predominantly high correlation coefficients between the waves observed with RPCMAG and ROMAP in all the visited area allow to draw conclusions about the plasma environment. Collective plasma oscillations occur on length-scales larger than the maximum orbiter-lander distance. Therefore, the wavelength of the observed waves must be also much larger than the maximum distance between orbiter and lander** and thus any spatial aliasing effects do not play any role - otherwise the correlation coefficients (and the required time shift to obtain max. correlation) would show a significant spatial variation. Hence, we conclude from the correlation analysis that the wavelengths have to be larger than 18 km.

Frequency distribution of the observed waves

The frequency of the waves is one key characterization parameter, as it reflects the processes that the plasma undergoes. For a dynamic frequency analysis within the complete descent and landing phase the magnetic field data have to be treated in a special way. As mentioned previously, first order Butterworth bandpasses with 10 mHz and 100 mHz corner frequencies have been applied twice (forward and backward in time in order to avoid phase shifts). Furthermore the complete time series are split into chunks of 1200 s intervals which are shifted forward by 60 s in each step. Each of these intervals is cut into 300 s wide windows which is shifted by only half window widths, namely 150 s, in order to achieve a reasonable overlap and to perform a statistical significant frequency analysis. Thus, each 1200 s interval is divided into 7 smaller intervals of 300 s, which are used to obtain averaged spectral information by summing up the individual results of the single windows. The chosen interval lengths turned out to be a suitable compromise between the low frequencies to be analyzed and the less data points available during SDL.

245 For the proper assessment of the estimated frequencies three different types of frequencies are determined from the datasets: First ROMAP and RPCMAG time series are investigated separately and the two individual frequencies of the maximum wave power are calculated using dynamic power spectral analyses during the mentioned intervals above. In addition a cross-spectral analysis is executed using both datasets together and the frequencies of the maximum cross power is determined as well. The three resulting histograms of the calculated frequency distributions are presented in Fig.7. **The figure includes several interesting features:** firstly, the observed frequency distributions for RPC-

MAG (green), ROMAP (red) and the maximum cross-power frequency (light-blue) show remarkable similarities. Secondly, there is no distinct single wave frequency but a broadband excitation in the 10-45 mHz range, not inconsistent with the *Richter et al. (2015)* results that reported magnetic field oscillations with a typical value of ~ 40 mHz. However, the most dominant frequencies measured by both instruments in parallel are in the order of 25 mHz, as can be seen in the cross-power frequency distribution without a doubt. Third, the ROMAP data exhibit a much higher spectral content in the band around 15 mHz. The appearance of maximum power at these frequencies is due to the frequency aliasing signature of PHILAE's flywheels which are mirrored into this frequency band. This disturbance, however, could not be eliminated as the exact frequencies are not known due to a lack of lander housekeeping parameters at SDL. Hence, we conclude that the RPCMAG data and the signal in the undisturbed frequency band of the ROMAP data show a very similar frequency distribution. This is doubtlessly reflected in the distribution of the frequency of maximum cross-power. For the further analysis we concentrate purely on this frequency of max cross-power. Furthermore we only use time intervals where the correlation of both datasets is larger than $R = 0.75$, where the coherence is larger as 0.75 as well and where the cross power spectral density (rms) is larger than $2700 \text{ nT}^2/\text{Hz}$ in order to select statistical significant intervals only.

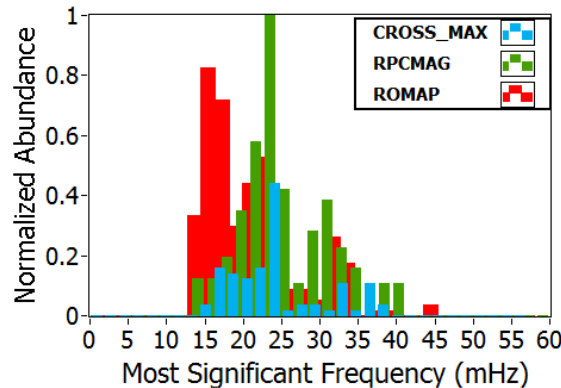


Figure 7. Normalized histograms (using 32 bins) of the most prominent frequencies for measurements by RPCMAG (green) and ROMAP (red). The flywheel-signature of PHILAE at ~ 15 mHz can clearly be identified. The blue histogram reflects the distribution of the frequencies at which the maximum cross power spectral density of both instrument datasets occurs.

Further information about the occurring frequencies of max cross-power is provided in Fig.8. Here the spatial frequency distribution in dependency of the orbiter-lander distance is displayed. For times just after separation no observations are available, because the ROMAP boom has not been deployed until 08:56 and ROMAP was therefore operating inside the ambient noise of PHILAE. Furthermore the early phase of the descent was characterized by only low wave activity causing problems in

determining PHILAE's attitude, as the attitude calculation - based on magnetic field measurements
280 - is only possible if significant, collective magnetic variations are present.

Nevertheless the plot reveals an interesting pattern. There seems to be a trend showing that lower frequencies appear at larger ROSETTA-PHILAE distances. However, as these measurement were made at different times, a purely temporal dependency - or a dependency of any other changing plasma entity - could be causing this finding as well.

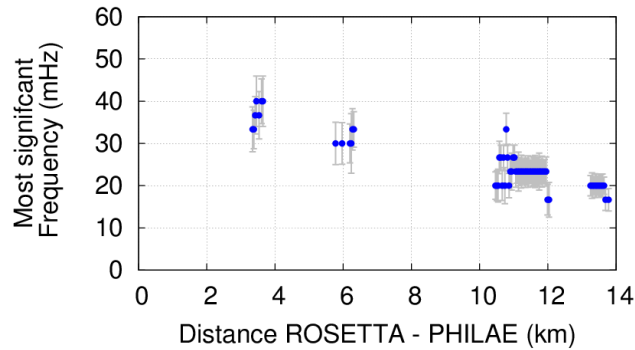


Figure 8. Profile of the most significant wave frequency (including gray error bars) versus the orbiter-lander distance. The frequency at which the cross-spectral density of RPCMAG and ROMAP measurements reaches a its maximum value is plotted against the distance between ROSETTA and PHILAE during descent.

285 As described by *Richter et al. (2015)* the waves are assumed to be generated by a cross-field-current instability. As both, the wave source as well as the two observing spacecraft are almost stationary in the nucleus rest frame (the velocities with respect to the CSEQ frame are in the order of 1 m/s) any Doppler shift between wave transmitter and receiver, which usually has to be taken into account when discussing waves in the streaming solar wind, need not to be considered here – the
290 wave generator and the observer are located in the same frame. Furthermore, the interaction region is too small and the interaction time too short to accelerate the wave-carrying medium to significant velocities that might require Doppler shift considerations. It should be mentioned here as well, that this short-term frequency distribution of the most prominent waves during SDL is similar to the one obtained by RPCMAG measurements made in the long-term comet observation phase between
295 August 2014 and March 2015.

Amplitudes of the observed waves

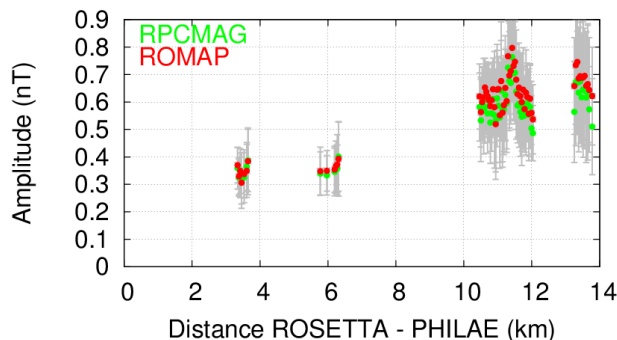


Figure 9. Amplitudes of magnetic fields observed by RPCMAG (green) and ROMAP (red) at the most significant frequencies plotted versus the orbiter-lander distance. The amplitudes represent the mean of all three components.

For a detailed amplitude analysis the time series of RPCMAG and ROMAP data have been analyzed in the frequency domain (Fig.9). Shown are the amplitudes of the RPCMAG (green) and ROMAP (red) signals, derived from the the Power Spectral Density $P(f)$ as average over the three components (Amplitude= $\frac{1}{3} \sum_{i=x,y,z} \sqrt{P_i(f_{\max}) \cdot \Delta f}$, with $\Delta f = 1/T$ and T duration of the used data interval) . The amplitudes represent again the waves at the frequencies of maximum cross power, displayed in spatial dependency of the orbiter-lander distance. **The 90% confidence intervals of the amplitude determination are displayed in gray as error bars for both instruments. They have been computed according to standard procedure described in Bendat and Piersol (1971) [Section 4.4].**

It can be seen, that both instruments detect the same variations in the signals. Especially the common temporal variations registered at about 11 km distance prove spatial coherence of the observed the plasma dynamics. This is consistent with the estimated coherence length of 48 km. In addition we know from the long-term observations that the 'singing of the comet' commenced at 100 km distance from the comet. Therefore, we regard an area of ~ 100 km extension as an upper limit for the diameter of the source region of the observed waves.

Furthermore it should be mentioned that the ROMAP signals were slightly larger for larger orbiter-lander distances **compared with the RPCMAG amplitudes**. This is exhibited even clearer in Fig.10, where the ratio of the ROMAP/RPCMAG amplitudes is plotted versus the orbiter-lander distance. This ratio does not show an unambiguous amplitude change with varying orbiter-lander distance, respectively lander-comet distance, as only less data and one descent profile is available. Nevertheless, the amplitudes in **the** vicinity of the comet seem to be up to $\sim 10\%$ larger than farther away. The amplitude ratio **ROMAP/RPCMAG** at e.g. 3.5 km orbiter-lander distance is about 1.0 ± 0.05 .

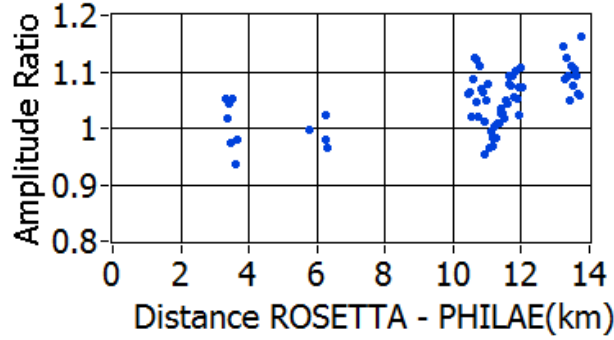


Figure 10. The ratio of the ROMAP/RPCMAG magnetic field amplitudes (from Fig.9) plotted versus orbiter-lander distance.

With increasing orbiter-lander distance, respectively decreasing lander-comet distance, the amplitude ratio rises continuously up to about 1.1 ± 0.05 at 13 km orbiter-lander distance. Despite the lack of multiple descent profiles available we tend to consider this increase as a significant change in amplitude ratio.

Phase relations and wavelength estimations

The relative phase shift of the waves measured at different locations is a key parameter for the estimation of the wavelength. This phase shift is calculated at the local frequency of maximum cross-power, derived from a cross-spectral analysis. The algorithm has been applied to all data available during the SDL segments using the parameters and thresholds mentioned above.

From the theoretical point of view the phase shift is identical for corresponding component-pairs $(B_x^{\text{ROMAP}}, B_x^{\text{RPCMAG}})$, $(B_y^{\text{ROMAP}}, B_y^{\text{RPCMAG}})$, and $(B_z^{\text{ROMAP}}, B_z^{\text{RPCMAG}})$. Therefore, the average of the phase shift $\Delta\varphi = \frac{1}{3} \sum_{i=x,y,z} \Delta\varphi_i$ will be used as the basis for the following considerations in order to derive a statistically significant result.

As a result of this phase analysis the relative phase shift $\Delta\varphi$ is plotted versus the orbiter-lander distance in Fig. 11. The phase shift is subject to certain spatio-temporal changes. For example at ~ 11 km distance an increased level of variation caused by temporal effects can be recognized, as already seen at the wave amplitude examination.

Due to the lack of scientifically usable data for the times where orbiter and lander were still connected (i.e. at 0 km distance) and where the ROMAP boom was still in its stowed positions, statements about phase shifts can only be made for ROSETTA/PHILAE distances between 3 km and 14 km. From Fig. 11 a linear decrease of the relative phase shift can be derived as a rough estimate for this range. A spatial phase drop of $\Delta\varphi/\Delta r \approx (1.44^\circ \pm 0.16^\circ)/\text{km}$ results. Here Δr denotes the

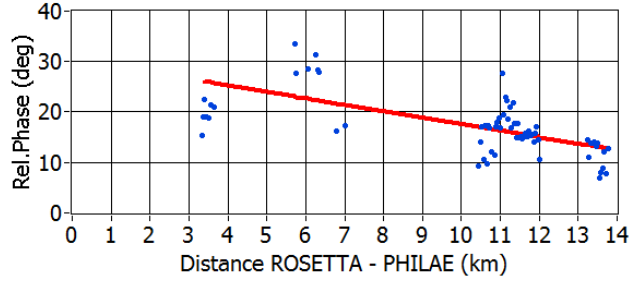


Figure 11. The phase shift between signals of RPCMAG and ROMAP (blue), taken at the frequency at which the maximum cross-spectral density occurs, versus the orbiter-lander distance. The red line represents the linear fit.

340 orbiter-lander distance. The general phase relation of a wave is given by $\varphi = \omega t - k r$. Thus, the phase difference $\Delta\varphi = \varphi_2 - \varphi_1$ of two waves with equal angular frequencies ω is given by $\Delta\varphi = k \cdot \Delta r$.

It has to be noted for the following estimation of the wavenumber and wavelength that these entities have to be regarded as projected wavenumber k_p and projected wavelength λ_p onto the actual connecting line between orbiter and lander. As seen in Fig.4 the direction of this connecting line is
 345 fairly constant during the descent. This means that **this direction can be regarded as constant for the calculation and interpretation of the wavenumber and wavelength. Thus any occurring variation of the phase shift of the wave packets is subject to a varying distance between the points of observation and not to a changing direction of this baseline.**

Thus, we get a projected wavenumber $k_p = (\Delta\varphi/\Delta r) \cdot 2\pi/360^\circ = (2.5 \pm 0.28) \cdot 10^{-5} \text{ m}^{-1}$ from
 350 the measured phase decrease presented above. From this we calculate a projected wavelength $\lambda_p = 2\pi/k_p = (251 \pm 31) \text{ km}$.

A more detailed wavelength study can be performed using not only the global estimated phase gradient $\Delta\varphi/\Delta r$ but the actual phase shifts $\Delta\varphi_j$ at all possible distance Δr_j . This leads to a distribution of all calculated projected wavelengths $(\lambda_p)_j = (360^\circ/\Delta\varphi_j) \cdot \Delta r_j$, presented in the histogram in Fig.12. It exhibits a broad distribution of a few hundred kilometers, with a calculated mean
 355 wavelength of $\langle \lambda_p \rangle = 278 \pm 19 \text{ km}$ as most probable wavelength. The related mean wavenumber is $\langle k_p \rangle = (2.3 \pm 0.2) \cdot 10^{-5} \text{ m}^{-1}$. The computed wavelengths in dependency of the orbiter-lander distance are presented in Fig.13.

The larger wavelengths, respectively smaller wavenumbers, being exhibited at larger distances are
 360 related to lower frequencies at larger distances as can be seen in Fig. 8. This interrelationship suggests a systematical dispersion relation between k_p and ω being discussed now.

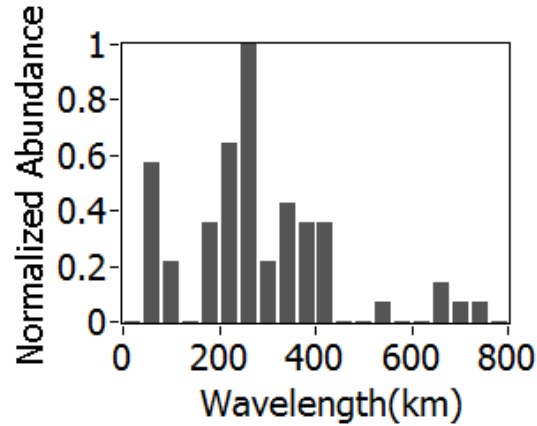


Figure 12. Normalized histogram (bin size: 40 km) of the estimated wavelengths, projected on the orbiter-lander connecting line.

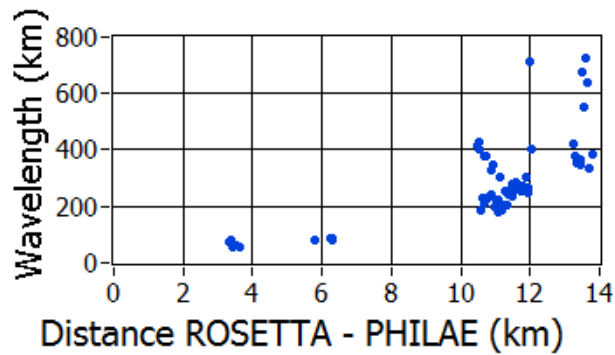


Figure 13. The estimated wavelengths, projected to the orbiter-lander connecting line, are plotted versus the orbiter-lander distance.

The dispersion relation

The combination of frequencies and wavelengths (respectively angular frequencies and wavenumber) in a common diagram, as exhibited in the plot of the calculated dispersion relation in Fig.14, eliminates any direct spatio-temporal dependency discussed above, and reveals a statement about the wave velocities. From the observations (blue) we derive the angular frequency $\omega = 2\pi f$ and the related modulus of the projected wavenumber $k_p = 2\pi/\lambda_p$. As the angular frequency shows a linear behavior w.r.t. the wavenumber, a linear fit (red) is added as well. The slope of the straight line, representing the group velocity $v_g = \partial\omega/\partial k_p$, has a constant value of (1.2 ± 0.3) km/s (derived from a linear fit).

The phase velocity $v_p = \omega/k$ varies with the wavenumber as the data are not represented by a straight line through the origin. For the most probable wavelength of $\lambda_p = 278$ km a phase velocity $v_p = 6.1$ km/s results. For e.g. $\lambda_p = 500$ km we derive a phase velocity of $v_p = 10.2$ km/s. These velocities are in the order of the values obtained from the plasma simulations in *Koenders et al.* (2016). For comparison the Alfvén-velocity computes as $v_A = B_0/\sqrt{\mu_0\rho} = (2.23 \pm 0.47)$ km/s, under the assumption of an average background magnetic field of $B_0 = (5.3 \pm 0.1)$ nT, a mass density $\rho = n \cdot m_{\text{H}_2\text{O}}$ of water ions, and a number density of $n \approx (150 \pm 30)$ cm^{-3} , taken as a rough estimate from RPCLAP measurements in October 2014 (*Edberg et al.*, 2015). Thus, the Alfvén-velocity is in the same order of magnitude as the velocity of the 'singing comet' waves.

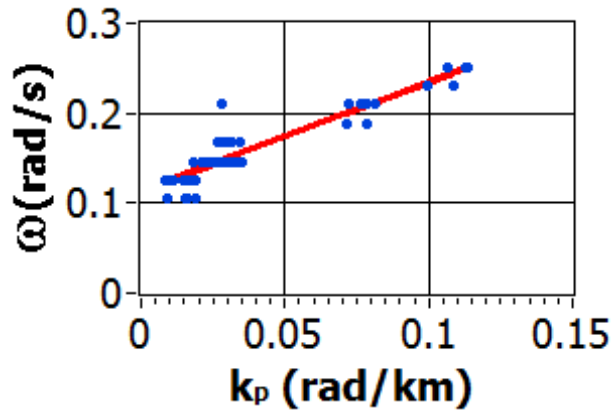


Figure 14. Derived dispersion relation (blue) including a linear fit (red). For the calculation the projected wavelength on the orbiter-lander connecting line and the related angular frequencies at which the maximum cross-power occurs have been used.

380 Additional wave properties derived from variance analyses

Using the minimum/maximum-variance analysis (MVA) additional wave properties have been obtained to complete the knowledge of the "singing comet" waves (*Senfft*, 2014). The analysis has been performed using moving windows of 300 s length with an overlap of 60 s for the complete SDL phase. RPCMAG and ROMAP datasets have been treated in the same way, only the flywheel disturbances at $\sim 15 - 18$ mHz in ROMAP data have been damped using a bandpass with a lower corner frequency of 15 mHz rather than 10 mHz as applied to the RPCMAG data. The resulting maximum variance directions are shown in Fig. 15, the minimum variance directions are plotted in Fig. 16. In both figures RPCMAG results are displayed in the top panels whereas ROMAP results are shown at the bottom. The azimuth represents the direction angle in degrees and the radius, respectively the length of the lines, is related to the eigenvalue ratios. The plots are color-coded in the following way: the blue lines represent the results of the complete MVA. The red lines mark

elliptically or more complex polarized waves only because the eigenvalue ratios for this subset are limited to $\lambda_{\max}/\lambda_{\text{med}} \geq 2$ and $\lambda_{\text{med}}/\lambda_{\min} \geq 3$. The yellow lines finally are related to circular polarized waves as the used eigenvalue ratios are confined by $\lambda_{\max}/\lambda_{\text{med}} \leq 1.3$ and $\lambda_{\text{med}}/\lambda_{\min} \geq 3$. The limiting ratio $\lambda_{\text{med}}/\lambda_{\min} \geq 3$ has been chosen as a compromise in order to avoid any interpretation of misleading noise patterns and to keep an adequate amount of datapoints.

From the two columns of Fig. 15 qualitatively the same directions of maximum variance can be deduced in both planes. Due to less usable ROMAP observations the ROMAP results are more sparse. However, the common maximum variance direction is centered at $\sim \pm 45^\circ$ around 90° to the CSEQ-z direction. This means the magnetic field oscillations mainly occur in the CSEQ-xy-plane. The left column of Fig.15 shows the distribution of the projected variance direction in the CSEQ-xy plane with the x-axis as a reference line. The blue pattern, representing results regardless of any eigenvalue constraints, is characterized by a quasi-homogeneous distribution, whereas the maximum variance of the elliptically or more complex polarized waves (red pattern) seems to have a weakly pronounced predominant direction at $\sim 140^\circ \pm 10^\circ$. Also circular waves (yellow), which are characterized by an eigenvalue ratio of $\lambda_{\max}/\lambda_{\text{med}} \sim 1$, seem to be present. But as the amount of events is very low, they are not considered as a predominant phenomenon in this context.

The temporal behavior of the maximum variance directions (not shown here), however, does not exhibit any striking feature, neither for ROMAP nor for the RPCMAG measurements.

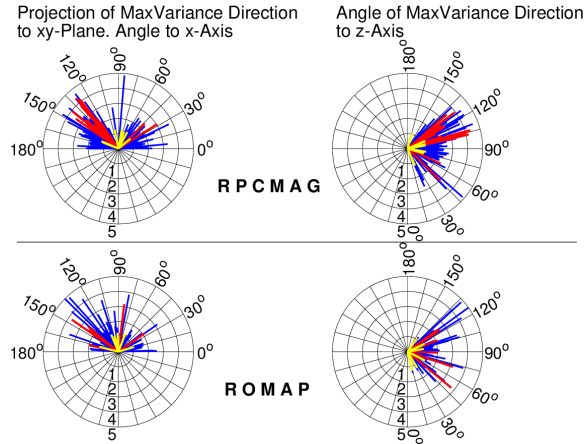


Figure 15. Distribution of **maximum** variance directions derived from RPCMAG (top) and ROMAP (bottom) data for the complete descent. Color coding — blue: all MVA results, red: elliptical/more complex polarization ($\lambda_{\max}/\lambda_{\text{med}} \geq 2$ and $\lambda_{\text{med}}/\lambda_{\min} \geq 3$), yellow: circular polarization ($\lambda_{\max}/\lambda_{\text{med}} \leq 1.3$ and $\lambda_{\text{med}}/\lambda_{\min} \geq 3$). The radial component represents the eigenvalue ratios.

The angle distribution of minimum variance directions, representing the wave propagation directions, can be obtained from Fig. 16. Also here a qualitative accordance between RPCMAG and ROMAP results can be seen. From RPCMAG we retrieve a projected angle of the most prominent

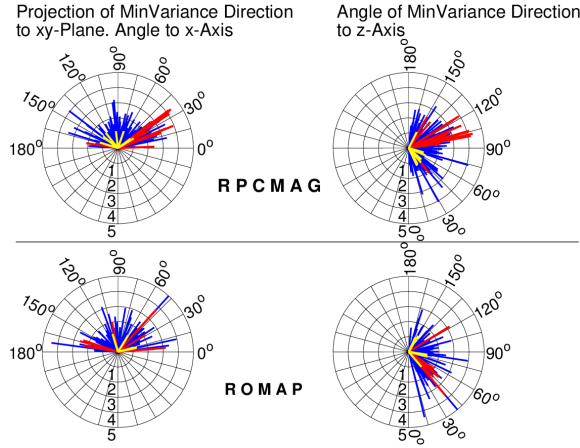


Figure 16. Distribution of **minimum** variance directions derived from RPCMAG (top) and ROMAP (bottom) data for the complete descent. Color coding — blue: all MVA results, red: elliptical/more complex polarization ($\lambda_{\max}/\lambda_{\text{med}} \geq 2$ and $\lambda_{\text{med}}/\lambda_{\min} \geq 3$), yellow: circular polarization ($\lambda_{\max}/\lambda_{\text{med}} \leq 1.3$ and $\lambda_{\text{med}}/\lambda_{\min} \geq 3$). The radial component represents the eigenvalue ratios.

elliptically or more complex polarized waves (red) onto the CSEQ-XY planes (left column) of about $20^\circ - 40^\circ$, respectively $200^\circ - 220^\circ$ (the MVA only yields directional information modulo $\pm 180^\circ$).

415 The analysis of ROMAP data yields a projected azimuth of about $165^\circ - 180^\circ$. Thus, there is a directional deviation of $\sim 30^\circ$ between both sets of observations. For the projected minimum variance direction onto the CSEQ-z axis (Fig.16, right column) we find angles of about $105^\circ - 120^\circ$ for RPCMAG detected waves and about $30^\circ - 45^\circ$ for ROMAP observations. Considering that the angles are located on a cone-shaped shell around the z-axis this results in a deviation of elevation between
420 both datasets of roughly 20° .

From these findings we calculate (0.68, 0.44, 0.34) as the average minimum variance direction in the CSEQ-System. Only eigenvalue ratios of $\lambda_{\text{med}}/\lambda_{\min} \geq 3$ have been used for this estimation.

This means that the main wave propagating direction during the descent points approximately in the diagonal in space direction from +x+y+z-Octant to the -x-y-z-Octant (or vice versa). Comparing
425 this with the orbiter-lander connecting line shown in Fig.4 we see, that this direction is quasi perpendicular to the wave propagation direction. This explains, why sometimes the wave-packets are seen first at ROMAP and sometimes first at RPCMAG.

Furthermore the propagation direction can be compared with the mean direction of the background magnetic field. From the three major magnetic field configurations stated in the 'joint observations
430 section' we calculate the mean directions of the magnetic field as $\langle \mathbf{B}_0/B_0 \rangle = (-0.77, -0.02, 0.64)$ for the interval 10:20 - 12:40 UTC, as $\langle \mathbf{B}_0/B_0 \rangle = (-0.35, -0.52, 0.78)$ between 12:50 and 16:00 UTC and as $\langle \mathbf{B}_0/B_0 \rangle = (-0.36, -0.82, 0.45)$ for the period 16:00 - 18:00 UTC. The conjunction of these findings with the results of the minimum variance analysis leads to angles between the mean

magnetic field direction and the wave propagation direction of $(111^\circ \pm 13^\circ)$, $(69^\circ \pm 10^\circ)$, $(147^\circ \pm 4^\circ)$
435 for the three time intervals above. This means that the major wave propagation direction is roughly
perpendicular to the main magnetic field direction.

The polarization analysis yields that elliptical or more complex modes are prevailing for all
transversal waves showing a significant propagation direction defined by $\lambda_{\text{med}}/\lambda_{\text{min}} \geq 3$. The hodo-
grams of these waves, however, do not show any prominent characteristics. There are neither purely
440 left-handed nor right-handed elliptical polarization patterns. Circular modes are present as well, but
the amount of these events is too low to be able to extract reliable statements. Also the rotational
sense of this polarization is highly variable and does not seem to follow any global principle.

6 Error Estimation

As completion of the parameter discussion an error estimation shall be given finally. We are concen-
445 trating on wave properties only, therefore neither instrument offsets nor the s/c bias fields play any
role. The influences of the orbiter reaction wheels have been eliminated, the disturbance of the lan-
der fly wheels was recognized but does not influence the analyses as it is outside the frequency band
of interest. Amplitudes and frequencies have been derived by the means of power spectral density
analyses using moving time windows and averaging over sub-windows as described above. Thus, we
450 have got seven degrees of freedom in our spectral calculations, which is for sure not ideal, but a suit-
able compromise, in order to get a reasonable frequency resolution under the given circumstances.

The crucial point is the phase and wavelength calculation. For this the relative timing of both mag-
netometer datasets has to be precise. With our knowledge of the data handling onboard ROSETTA
and PHILAE, we know that the timing accuracy is better than ± 1 s (conservative assessment). Trans-
455 lating this into a phase error at 25 mHz yields an uncertainty of $\pm 9^\circ$. A calculation of the most
probable wavelengths derived from distributions taking $\pm 9^\circ$ phase offsets into account yields wave-
lengths of 223 km and 313 km accordingly.

Furthermore a conservative guess of the relative position error of 100 m would cause an additional
uncertainty in wavelength of 1 % at 10 km distance.

460 As final result we hence obtain an assured value for projected wavelength in the order of about
300 km, derived from the joint RPCMAG-ROMAP measurements. This clearly proves the assump-
tion made early that the considered region of observation is small in relation to the occurring wave-
lengths.

The considered phase error of $\pm 9^\circ$ causes also an uncertainty in the derived wave velocities. The
465 nominal group velocity of 1.2 km/s would vary between 1.1 km/s and 1.4 km/s under the influence
of the stated phase error.

A final remark on the variability of the obtained parameters shall be made here. During the con-
sidered descent and landing phase of PHILAE, which lasted about 9 hours, the comet performed a

3/4-rotation. From long-term measurements it is known, that e.g. the outgassing rate, respectively
470 also the particle density, is modulated not only with the comet rotation period but also with the half
period of 6.2 h (*Hässig et al.*, 2015). This means that also the close cometary environment is influ-
enced by this variability. Furthermore there is an asymmetry in outgassing between the northern and
southern hemisphere. Typical outflow velocities of the cometary neutrals are in the order of ~ 1 km/s
(as a snapshot measurement 0.68 km/s is reported by *Gulkis et al.* (2015)). A Typical velocity of the
475 undisturbed solar wind is in the order of 400 km/s. It will be slowed down in the close vicinity of the
comet due to ion pickup and mass-loading. All these processes vary on different spatial and temporal
scales leading to variations seen in our separated observations and in the derived parameters.

The limitations originated in the equipment available has to be considered as well. We have only
two spacecraft at our disposal. Both are permanently moving, one is approaching a rotating comet
480 with unknown properties. This situation complicates the interpretation of those results, which have
to be derived from joint measurements, i.e., phase shifts, wavelengths and velocities. Hence the
distinction between spatial and temporal effects stays ambiguous for these parameters. For proper
determination of the real wavelength methods like the wave-telescope (*Glassmeier et al.*, 2001) using
4 spacecraft would be needed, in order to remove the projection bias.

485 7 Conclusions

With the ROSETTA mission we were able to perform long-term magnetic field measurements dur-
ing the long approach phase to 67P/C-G, and at 67P/C-G during landing of PHILAE. During SDL
we had the unique opportunity to conduct joint measurement with two magnetometers, RPCMAG
and ROMAP, at different, varying locations. These joint measurements confirm the detection of
490 low-frequency waves with frequencies around $\sim 20 - 50$ mHz, amplitudes up to ~ 3 nT, and the es-
timated wavelength of (*Richter et al.*, 2015) in the order of a few hundred kilometers. Furthermore
we estimate an upper extension limit of the source region as about 100 km diameter and calculate
the coherence length as roughly 48 km. Due to the small extension of the source region **with respect**
to the wavelength we conclude that the wave source can be considered as quasi point-shaped.

495 **The joint measurements also allowed to calculate the mean projected wavenumber ($\langle k_p \rangle =$
 $(2.3 \pm 0.2) \cdot 10^{-5} \text{ m}^{-1}$.) and the dispersion relation - the relationship between observed pulsatances
and wavenumbers. From this linear dispersion relation we were able to derive a constant group
velocity $v_g = (1.2 \pm 0.3) \text{ km/s}$ and the phase velocity $v_p = (6.1 \pm 0.8) \text{ km/s}$ for a wave of 278 km
wavelength.**

500 According to the general antenna theory (*Wheeler*, 1959) the near field region of a radiator is lo-
cated inside a sphere of $r_{nf} = \lambda$, whereas the far field region is located at outside $r \gg 2\lambda$. This con-
dition applies for short antennas with dimensions $D \leq \lambda/2$, whereas for larger antennas the border
of near field region is given by the Fraunhofer length $r_f = 2D^2/\lambda$. In the present case the extension

of the source region is in the order of half of the wavelength. Thus, the transition region between
505 near field and far field is somewhere between 71 km and 278 km for a mean wavelength of 278 km.
This implies that all observations during SDL were made in the near field region.

The dominating wave propagation direction can be found roughly along the diagonal in space
direction from the CSEQ (+x+y+z)-Octant to the CSEQ (-x-y-z)-Octant (or vice versa, due to
the MVA-ambiguity). Furthermore the mean propagation direction of the low-frequency waves is
510 roughly perpendicular to the local magnetic background field.

It has been demonstrated Fig.(2) that the "singing comet" waves could be observed from August
2014 until March 2015, corresponding to heliocentric distances between 3.6 AU and 2.0 AU and to
outgassing rates between $(1.5 - 4.5) \cdot 10^{26} \text{ s}^{-1}$ accordingly. Afterward the waves vanished at still
decreasing heliocentric distances. The perihelion at 1.3 AU was reached in August 2015. The waves
515 reappeared finally in Spring 2016 at distance of roughly 2.6 AU. A detailed long-term investigation of
the temporal and spatial properties of the "singing comet" is not part of this work as we intentionally
concentrated on the SDL phase. Such a study is, however, already in preparation by Goetz et al.

We are heading to the end of the successful ROSETTA mission in September 2016, where final
RPCMAG observations will be made along the planned and controlled descent of the ROSETTA
520 orbiter down to 67P/C-G.

Acknowledgements. The RPCMAG and ROMAP data will be made available through the PSA archive of ESA
and the PDS archive of NASA. Rosetta is a European Space Agency (ESA) mission with contributions from its
member states and the National Aeronautics and Space Administration (NASA). The work on RPCMAG and
ROMAP was financially supported by the German Ministerium für Wirtschaft und Energie and the Deutsches
525 Zentrum für Luft- und Raumfahrt under contract 50QP 1401. We thank the European taxpayers for the kind
support of our space research. All computations concerning the s/c position and orientation have been calculated
with use of the SPICE software developed by NASA's NAIF team. We thank K.C. Hansen for providing two
values for the gas production rate which were extracted from a plot of a talk given at the ROSETTA SWT
meeting at ESAC in December 2015. Portions of this research were performed at the Jet Propulsion Laboratory,
530 California Institute of Technology under contract with NASA. We are indebted to the whole Rosetta Mission
Team, SGS, and RMOC for their outstanding efforts making this mission possible. We express our sincere
gratitude to the referees of this paper who contributed significantly to the finishing touch of this publication.

References

- Acton, C.H.: Ancillary data services of NASA's navigation and ancillary information facility, *Planet. Space Sci.* 44(1), 65-70, doi:10.1016/0032-0633(95)00107-7, 1996.
- 535 Auster, H.-U., Apathy, I., Berghofer, G., Remizov, A., Roll, R., Fornacon, K.-H., Glassmeier, K.-H., Haerendel, G., Hejja, I., Kührt, E., Magnes, W., Moehlmann, D., Motschmann, U., Richter, I., Rosenbauer, H., Russell, C.T., Rustenbach, J., Sauer, K., Schwingenschuh, K., Szemerey, I., and Waesch, R.: ROMAP: ROSETTA Magnetometer and Plasma Monitor, *Space Sci. Rev.* 128(1-4), 221-240, doi:10.1007/s11214-006-9033-x, 540 2007.
- Auster, H.-U., Apathy, I., Berghofer, G., Fornacon, K.-H., Remizov, A., Carr, C., Güttler, C., Haerendel, G., Heinisch, P., Hercik, D., Hilchenbach, M., Kührt, E., Magnes, W., Motschmann, U., Richter, I., Russell, C.T., Przyklenk, A., Schwingenschuh, K., Sierks, H., and Glassmeier, K.-H.: The nonmagnetic nucleus of comet 67P/Churyumov-Gerasimenko, *Science* 349(6247), doi:10.1126/science.aaa5102, 2015.
- 545 Bendat, J., Piersol, A.: Random Data: Analysis and Measurement Procedures, *WILEY-INTERSCIENCE*, 1971.
- Biele, J., Ullamec, S., Maibaum, M., Roll, R., Witte, L., Jurado, E., Muñoz, P., Arnold, W., Auster, H.-U., Casas, C., Faber, C., Fantinati, C., Finke, F., Fischer, H.-H., Geurts, K., Güttler, C., Heinisch, P., Herique, A., Hviid, S., Kargl, G., Knapmeyer, M., Knollenberg, J., Kofman, W., Kömle, N., Kührt, E., Lommatsch, V., Mottola, S., Pardo de Santayana, R., Remeteau, E., Scholten, F., Seidensticker, K. J., Sierks, H., and Spohn, 550 T.: The landing(s) of Philae and inferences about comet surface mechanical properties, *Science* 349(1), doi:10.1126/science.aaa9816, 2015
- Bieler, A., Altwegg, K., Balsiger, H., Berthelier, J.-J., Calmonte, U., Combi, M., De Keyser, J., Fiethe, B., Fougere, N., Fuselier, S., Gasc, S., Gombosi, T., Hansen, K., Hässig, M., Huang, Z., Jäckel, A., Jia, X., Le Roy, L., Mall, U.A., Rème, H., Rubin, M., Tenishev, V., Tóth, G., Tzou, C.-Y., and Wurz, P.: Comparison of 3D kinetic and hydrodynamic models to ROSINA-COPS measurements of the neutral coma of 555 67P/Churyumov-Gerasimenko, *A&A*(583), A7, doi:10.1051/0004-6361/201526178, 2015.
- Butterworth, S.: On the Theory of Filter Amplifiers, *Wireless Engineer*(7), 536-541, 1930.
- Carr, C., Cupido, E., Lee, C.G.Y., Balogh, A., Beek, T., Burch, J.L., Dunford, C.N., Eriksson, A.I., Gill, R., Glassmeier, K.-H., Goldstein, R., Lagoutte, D., Lundin, R., Lundin, K., Lybakk, B., Michau, J.L., Musmann, 560 G., Nilsson, H., Pollock, C., Richter, I., and Trotignon, J.G.: RPC: The Rosetta Plasma Consortium, *Space Sci. Rev.* 128(1-4), 629-674, doi:10.1007/s11214-006-9136-4, 2007.
- Edberg, N. J. T., Eriksson, A. I., Odelstad, E., Henri, P., Lebreton, J.-P., Gasc, S., Rubin, M., André, M., Gill, R., Johansson, E. P. G., Johansson, F., Vigren, E., Wahlund, J. E., Carr, C. M., Cupido, E., Glassmeier, K.-H., Goldstein, R., Koenders, C., Mandt, K., Nemeth, Z., Nilsson, H., Richter, I., Wieser, G. S., Szego, K., and 565 Volwerk, M.: Spatial distribution of low-energy plasma around comet 67P/CG from Rosetta measurements, *Geophys. Res. Lett.* 42(11), 4263-4269, doi:10.1002/2015GL064233, 2015.
- Glassmeier, K.-H., Coates, A.-J., Acuña, M.-H., Goldstein, M.-L., Johnstone, A.-D., and Neubauer, F.-M.: Spectral characteristics of low-frequency plasma turbulence upstream of Comet P/Halley, *J. Geophys. Res.* 94(37), doi:10.1029/JA094iA01p00037, 1989.
- 570 Glassmeier, K.-H., and Neubauer, F. M.: Low-Frequency Electromagnetic Plasma Waves at Comet P/Grigg-Skjellerup: Overview and Spectral Characteristics, *J. Geophys. Res.* 98(A12), 20921-20935, doi:10.1029/93JA02583, 1993.

- Glassmeier, K.-H. , Motschmann, U., Dunlop, M., Balogh, A., Acuña, M.H., Carr, C., Musmann, G., Fornacon, K.-H., Schweda, K., Vogt, J., Georgescu, E., and Buchert, S.: Cluster as a wave telescope – first results from the fluxgate magnetometer, *Ann. Geophys.* 19, 1439-1447, 2001.
- 575 Glassmeier, K.-H., Boehnhardt, H., Koschny, D., Kührt, E., and Richter, I.: The Rosetta Mission: Flying Towards the Origin of the Solar System, *Space Sci. Rev.* 128(1-4), 1-21, doi:10.1007/s11214-006-9140-8, 2007a.
- Glassmeier, K.-H., Richter, I., Diedrich, A., Musmann, G., Auster, U., Motschmann, U., Balogh, A., Carr, C., Cupido, E., Coates, A., Rother, M., Schwingenschuh, K., Szegö, K., and Tsurutani, B.T.: RPC-MAG The Fluxgate Magnetometer in the ROSETTA Plasma Consortium, *Space Sci. Rev.* 128(1-4), 649-670, doi:10.1007/s11214-006-9114-x, 2007b.
- 580 Gulkis, S., Allen, M., von Allmen, P., Beaudin, G., Biver, N., Bockelée-Morvan, D., Choukroun, M., Crovisier, J., Davidsson, B.J.R., Encrenaz, P., Encrenaz, T., Frerking, M., Hartogh, P., Hofstadter, M., Ip, W.-H., Janssen, M. Jarchow, C., Keilm, S., Lee, S., Lellouch, E., Leyrat, C., Rezac, L., Schloerb, F.P., Spilker, T.: Subsurface properties and early activity of comet 67P/Churyumov-Gerasimenko, *Science* 347(6220), doi:10.1126/science.aaa0709, 2015.
- 585 Hässig, M., Altwegg , K., Balsiger, H., Bar-Nun, A., Berthelier, J. J., Bieler, A., Bochsler, P., Briois, C., Calmonte, U., Combi, M., De Keyser, J., Eberhardt, P., Fiethe, B., Fuselier, S. A., Galand, M., Gasc, S., Gombosi, T. I., Hansen, K. C., Jäckel, A., Keller, H. U., Kopp, E., Korth, A., Kührt, E., Le Roy, L., Mall, U., Marty, B., Mousis, O., Neefs, E., Owen, T., Rème, H., Rubin, M., Sémon, T., Tornow, C. , Tzou, C.-Y., Waite, J. H., Wurz, P.: Time variability and heterogeneity in the coma of 67P/Churyumov-Gerasimenko, *Science* 347(6620), doi:10.1126/science.aaa0276, 2015.
- 590 Heinisch, P., Auster, H.-U., Richter, I., Hercik, D., Jurado, E., Garmier, R., Güttler, C., and Glassmeier, K.-H.: Attitude-reconstruction of ROSETTA's lander PHILAE using two-point magnetic field observations by ROMAP and RPC-MAG, *Acta Astronautica*, doi:10.1016/j.actaastro.2015.12.002, 2015, in press.
- 595 Heinisch, P., Finke , F.: Reconstructing Philae's flight: Philae's two hour flight from Agilkia to Abydos, *ESA*, 2015, [http://www.esa.int/spaceinvideos/Videos/2015/11/Reconstructing_Philae_s_flight].
- Koenders, C., Perschke, C., Glassmeier, K.H., Goetz, C., Richter, I., Motschmann, U.: Low-Frequency Waves at Comet 67P/Churyumov-Gerasimenko: Observations Compared to Numerical Simulations, *A&A*, 2016, **submitted (already recommended for publication after 1. revision)**
- 600 Jurado, E., Martin, T., Canalias, E., Blazquez, A., Garmier, R., Ceolin, T., Gaudon, P., Delmas, C., Biele, J., Ulamec, S., Remeteau, E., Torres, A., Laurent-Varin, J., Dolives, B., Herique, A., Roger, Y., Kofman, W., Jorda, L., Zakharov, V., Crifo, J.-F., Rodionov, A., Heinisch, P., Vincent, J.-B.: Rosetta Lander Philae: Flight Dynamics analyses for Landing Site Selection and Post- Landing Operations, *Acta Astronautica*, doi:10.1016/j.actaastro.2016.03.030, 2016
- 605 Neubauer, F.M., Glassmeier, K.-H., Pohl, M., Raeder, J., Acuna, M.H., Burlaga, L.F., Ness, N.F., Musmann, G., Mariani, F., Wallis, M.K., Ungstrup, E., and Schmidt, H.U.: First results from the Giotto magnetometer experiment at comet Halley, *Nature* 321(6067s), 352-355, doi:10.1038/321352a0, 1986.
- 610 Neubauer, F.M., et al.: First results from the Giotto magnetometer experiment during the 26P/Grigg-Skjellerup encounter, *A&A* 268(L5-L8), 1993.

- Richter, I., Koenders, C., Glassmeier, K.-H., Tsurutani, B.T., and Goldstein, R.: Deep Space 1 at comet 19P/Borrelly: Magnetic field and plasma observations, *Planet. Space Sci.*, 59(8), 691-698, doi:10.1016/j.pss.2011.02.001, 2011.
- 615 Richter, I., Koenders, C., Auster, H.-U., Frühauff, D., Götz, C., Heinisch, P., Perschke, C., Motschmann, U., Stoll, B., Altwegg, K., Burch, J., Carr, C., Cupido, E., Eriksson, A., Henri, P., Goldstein, R., Lebreton, J.-P., Mokashi, P., Nemeth, Z., Nilsson, H., Rubin, M., Szegő, K., Tsurutani, B. T., Vallat, C., Volwerk, M., and Glassmeier, K.-H.: Observation of a new type of low frequency waves at comet 67P/Churyumov-Gerasimenko, *Ann. Geophys.*, 33, 1031-1036, doi:10.5194/angeo-33-1031-2015, 2015.
- 620 Rubin, M., Koenders, C., Altwegg, K., Combi, M.R., Glassmeier, K.-H., Gombosi, T.I., Hansen, K.C., Motschmann, U., Richter, I., Tenishev, V.M., Tóth, G.: Plasma environment of a weak comet – Predictions for Comet 67P/Churyumov-Gerasimenko from multifluid-MHD and Hybrid models, *Icarus* 241, 38-49, doi:10.1016/j.icarus.2014.07.021, 2014.
- Senfft, M.: Rosetta blog: The singing comet, *ESA*, published at
- 625 [<http://blogs.esa.int/rosetta/2014/11/11/the-singing-comet/>], 2014
- Sierks, H., et al.: Rosetta news: Philae descent images, *ESA*, published at
- [http://www.esa.int/esatv/Videos/2015/05/Rosetta_news/Philae_descent_images], 2015
- Smith, E.J., Tsurutani, B.T., Slavin, J.A., Jones, D.E., Siscoe, G.L., Asoka Mendis, D.: International cometary explorer encounter with Giacobini-Zinner: magnetic field observations, *Science* 232(382-385), 1986.
- 630 Volwerk, M., Glassmeier, K.-H., Delva, M., Schmid, D., Koenders, C., Richter, I., and Szegő, K.: A comparison between VEGA 1, 2 and Giotto flybys of comet 1P/Halley: implications for Rosetta, *Ann. Geophys.*, 32, 1441-1453, doi:10.5194/angeo-32-1441-2014, 2014
- Wheeler, H.A.: The Radian Sphere Around a Small Antenna, 47, *Proceedings of the IRE, Institute of Radio Engineers*, 47, 1325-331, 1959.